Supplementary Information for

High Piezoelectric Property with Exceptional Stability in Self-Poled Ferroelectric Films

Lisha Liu[1,#,*], Jiaojiao Yi[2,#,*], Kun Xu[3,4,#], Zhen Liu[1], Mingmeng Tang[1], Le Dai[1], Xuan Gao[1], Yang Liu[1], Shuhao Wang[1], Zhang Zhang[1], Liang Shu[5], Jing-Feng Li[5], Shujun Zhang[6,*], Yaojin Wang[1,*]

[1]School of Materials Science and Engineering, Nanjing University of Science and Technology, Nanjing 210094, Nanjing, China.

[2]Laboratory of Advanced Multicomponent Materials, School of Mechanical Engineering, Jiangsu University of Technology, Changzhou 213001, China.

[3]Department of Mechanical Engineering, Stanford University, Palo Alto 94305, United States.

[4]National Center for Electron Microscopy in Beijing, School of Materials Science and Engineering, Tsinghua University, Beijing 100084, China.

[5]State Key Laboratory of New Ceramics and Fine Processing, School of Materials Science and Engineering, Tsinghua University, Beijing 100084, China.

[6]Institute of Superconducting and Electronic Materials, Faculty of Engineering and Information Sciences, University of Wollongong, Wollongong 2522, Australia.

[#]These authors contributed equally to this work

*Corresponding authors. Emails: lishaliu@njust.edu.cn (L.L.); yijiaojiao2006@163.com (J. Y.); shujun@uow.edu.au (S.Z.); yjwang@njust.edu.cn (Y.W.).

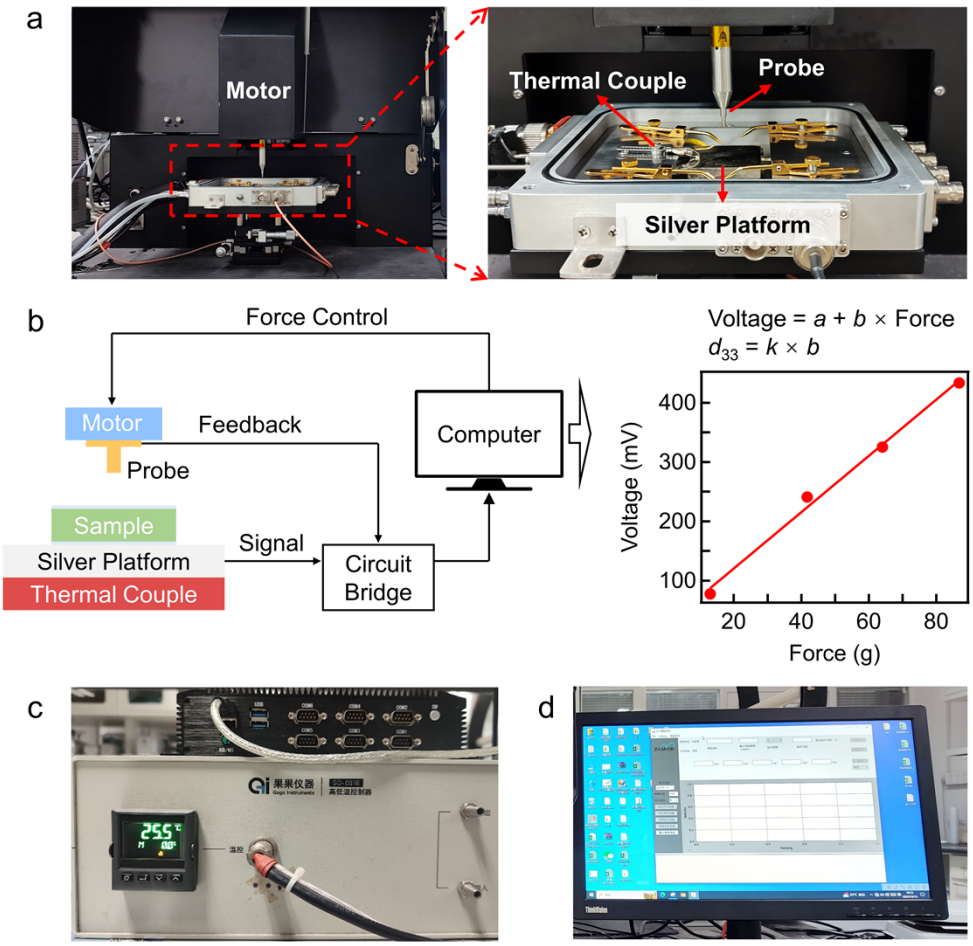

Supplementary Fig. 1. a, Experimental setup for measuring the direct $d_{33,d}$ of thin films. The samples are placed on the silver platform. **b,** Schematic diagram of the measurement circuit and output voltage versus applied force for fitting the $d_{33,d}$. The forces are applied in linear sequence of 20, 40, 60, and 80 g. The equations on the top-right corner provide a basic explanation of the measuring principle of the system. The constant k is calibrated by an internal standard sample at each measurement. **c,** Temperature controller LRT 001 (Gogo Instruments Technology, Shanghai, China) used for heating the silver platform for *in situ* high temperature measurements. The operando temperatures of the sample surface and the silver platform are recorded simultaneously using a *K*-type thermocouple (See Methods). **d,** Software for controlling the applied force and collecting the output signals.

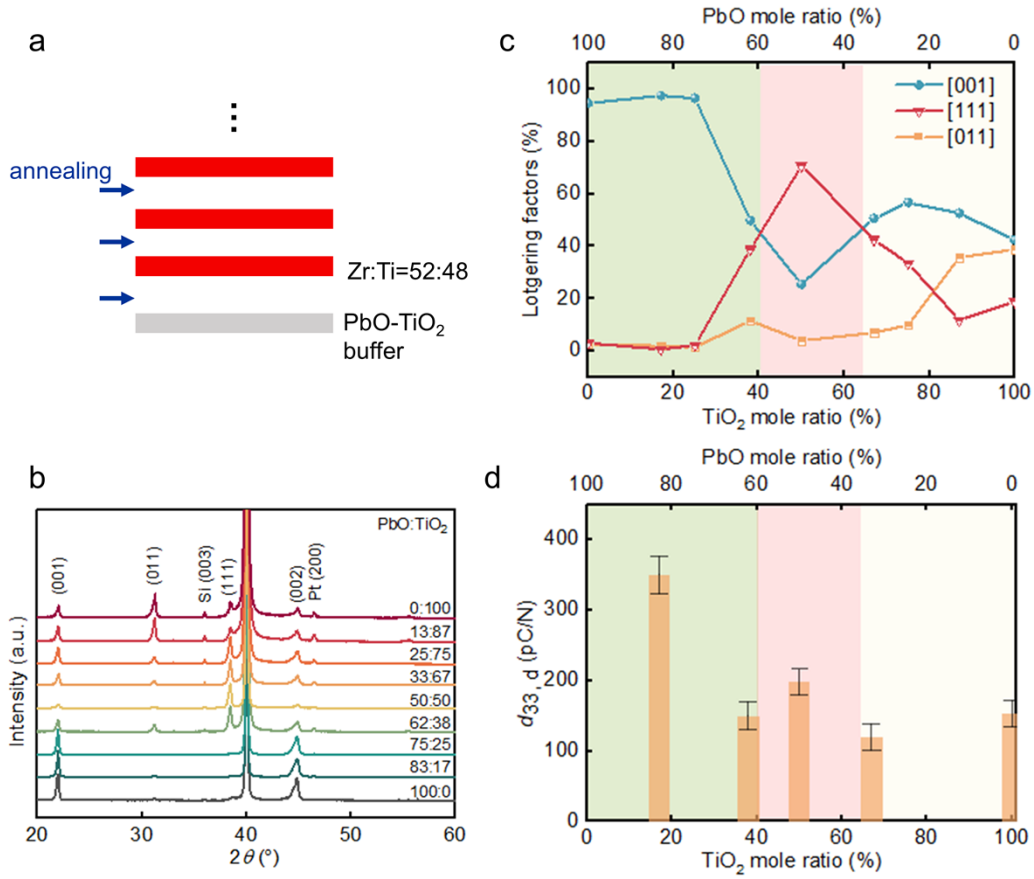

Supplementary Fig. 2. Texture construction through PbO-TiO_2 buffer layers. a, The buffer layers and PZT layers are deposited with a layer-by-layer annealing process as indicated by the blue arrows. Notably, the buffer is used for every ten PZT layers. **b,** XRD patterns of 1 μm-thick PZT films using buffer with different ratios of PbO-TiO_2, showing a smooth transition from [001], [111], to [011] texture. **c,** The Lotgering factors of [001], [111], and [011] textures. **d,** Piezoelectricity of selected PZT films at varied PbO/TiO_2 ratios. It is noticeable that smaller $d_{33,d}$ values are observed at the texture transition point where a lower texture is present (e.g., PbO-TiO_2 with 33:67 ratio). It is, thereby, deducible that texture enhancement benefits the increased $d_{33,d}$,

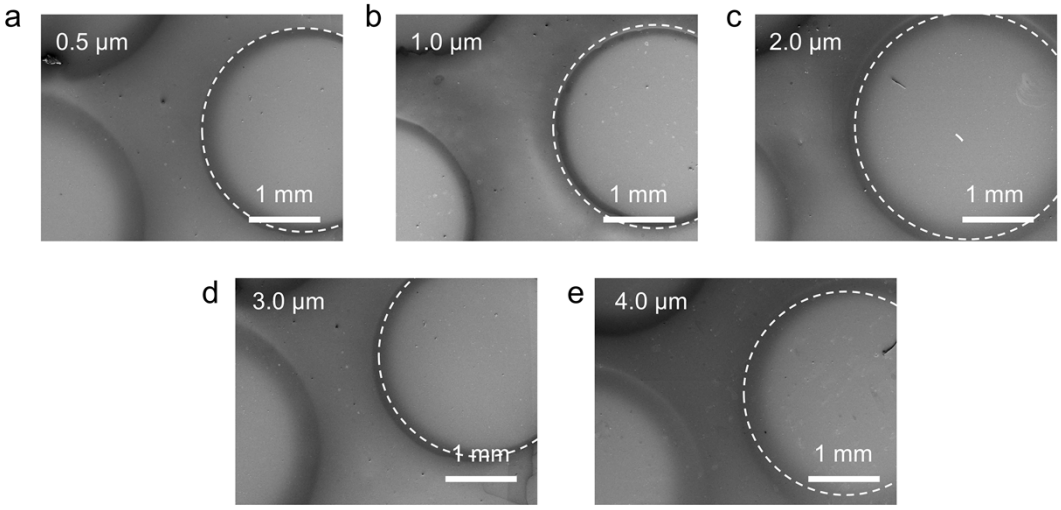

Supplementary Fig. 3. Scanning electron microscopy (SEM) images of high-quality, crack-free PZT films with varying thicknesses. **a,** 0.5 μm. **b,** 1 μm. **c,** 2 μm. **d,** 3 μm. **e,** 4 μm. The bright circular regions represent surface Pt electrodes with a diameter of 2.5 mm.

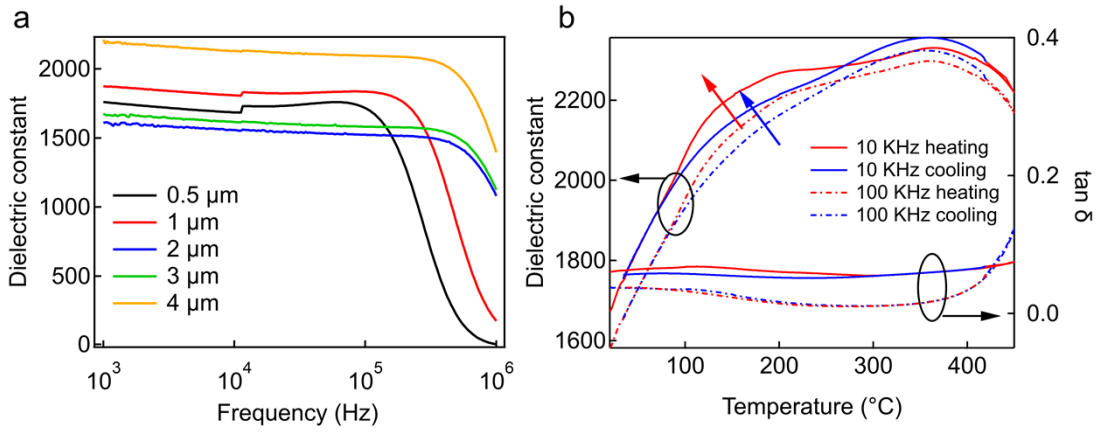

Supplementary Fig. 4. a, Frequency-dependent dielectric constant of the studied PZT film with thicknesses of 0.5, 1, 2, 3, and 4 μm. **b**, Temperature- and frequency-dependent dielectric constant and loss of the 2 μm-thick film. As shown in panel a, the dielectric constant ranges from 1610 and 2180 at a frequency of 1 kHz. These high values are attributed to the dense structure and pronounced texture of the PZT films at the morphotropic phase boundary (MPB). The dielectric constant increases with film thickness in the 2-4 μm range, contributing to the enhanced piezoelectricity observed with thicker films, as discussed in the main text. The 0.5 and 1 μm-thick films did not show smaller dielectric constants than the 2 and 3 μm-thick films and possess different trend in the frequency range above 100 kHz, likely due to their reduced texture degree or different electrical features. This discrepancy is also reflected in their *P-E* hysteresis characteristics. In panel b, for the representative 2 μm-thick film, the room temperature dielectric constant is consistent with that shown in panel a. Notably, frequency-dispersion behavior (red and blue arrows) is observed, which is a characteristic of relaxor-like ferroelectrics[1,2], and may be attributed to the reduced domain size in the nanoscale range of ~10 nm (the grain size of the studied thin film is about ~100 nm and the domain size is proportional to the square root of grain size[3]). This relaxor-like behavior may partially account for the outstanding dielectric constant.

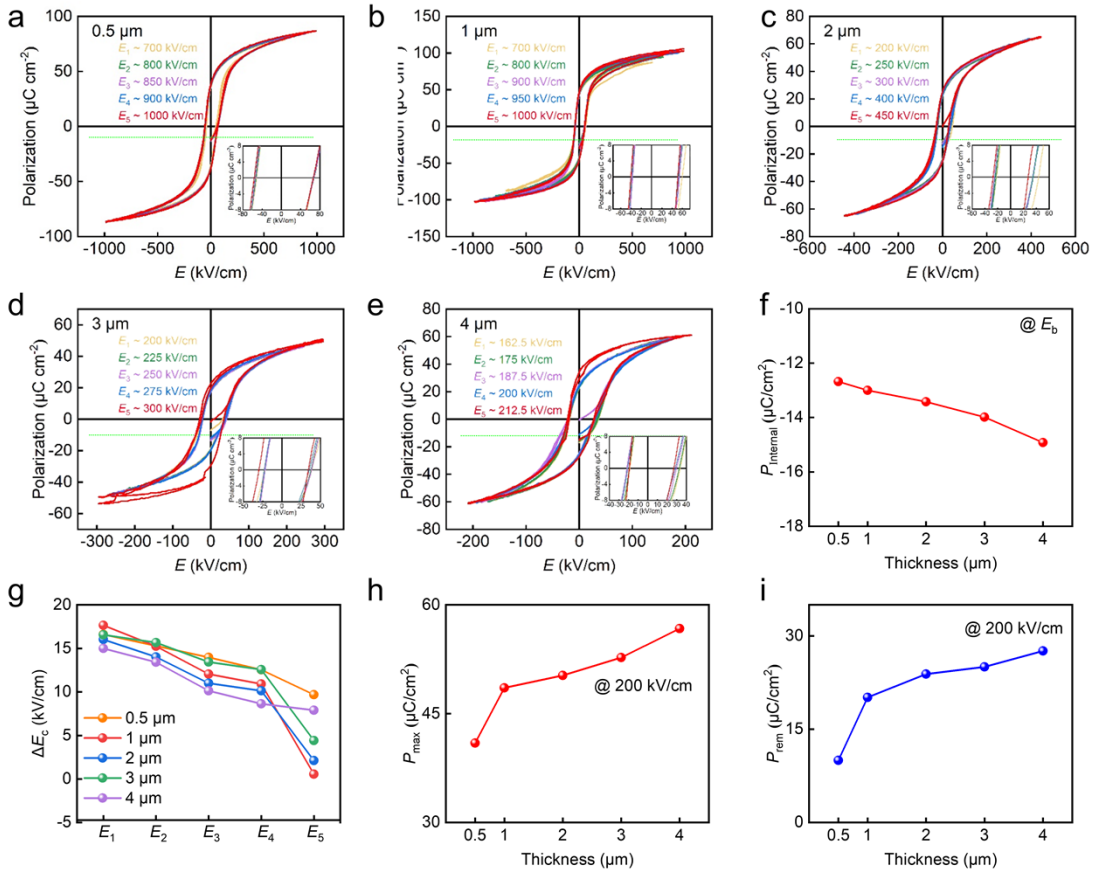

Supplementary Fig. 5. a-e, *P*-*E* loops for films with thicknesses of 0.5, 1, 2, 3, and 4 μm at respective fields ranging from E_1 to E_5 as marked. Each inset at the bottom-right shows enlarged view near the $+E_c$ and $-E_c$, illustrating the internal bias, if any, at respective applied external electric field. Each film set exhibits an initial polarization during the first measurement cycle, with the varying initial polarization values indicated by horizontal dashed green lines. **f,** Initial polarization values for different film sets at their breakdown fields, with the maximum value reaching –15 μC/cm^2, indicating the initial polarization alignment. **g,** Internal bias as a function of increasing applied external field (E_1 to E_5 as shown in panels a-e) for different film sets. Notably, a reduction of the internal bias with increasing applied external fields is observed, consistent with the PFM results, indicating a relatively easy polarization switching in the studied self-poled films. **h and i,** Maximum polarization (P_{max}) and remnant polarization (P_{rem}) at a fixed field of 200 kV/cm for films with increasing thicknesses. It is evident that at the same electric field of 200 kV/cm, remnant polarization increases with film thickness, correlating well with the increasing $d_{33,d}$ with greater thicknesses.

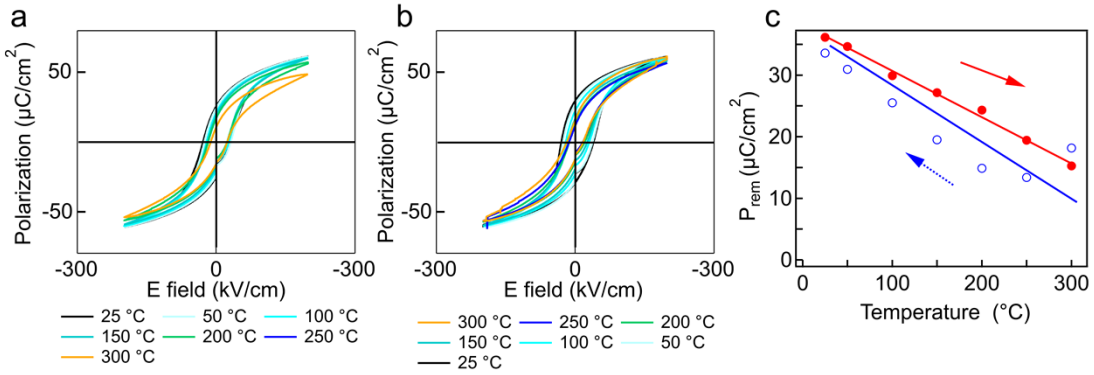

Supplementary Fig. 6. a and **b**, Temperature-dependent *P*-*E* loops during heating for as-prepared PZT film with 4 μm in thickness, up to its Curie temperature (i.e., 350 °C), and subsequently cooling down to room temperature. **c,** Temperature-dependent remnant polarizations (P_{rem}) extracted from the *P*-*E* loops measured during heating and cooling. P_{rem} decreases with increasing temperature and recovers upon cooling. At 350 °C (the Curie temperature), the loop becomes *broad*, indicating a leaky behavior induced by space charge at elevated temperature, and is therefore excluded from the figure. Notably, the heat treatment results in a difference in the *P*-*E* loop and the resultant P_{rem} value at the same temperature for the heating and cooling cycle.

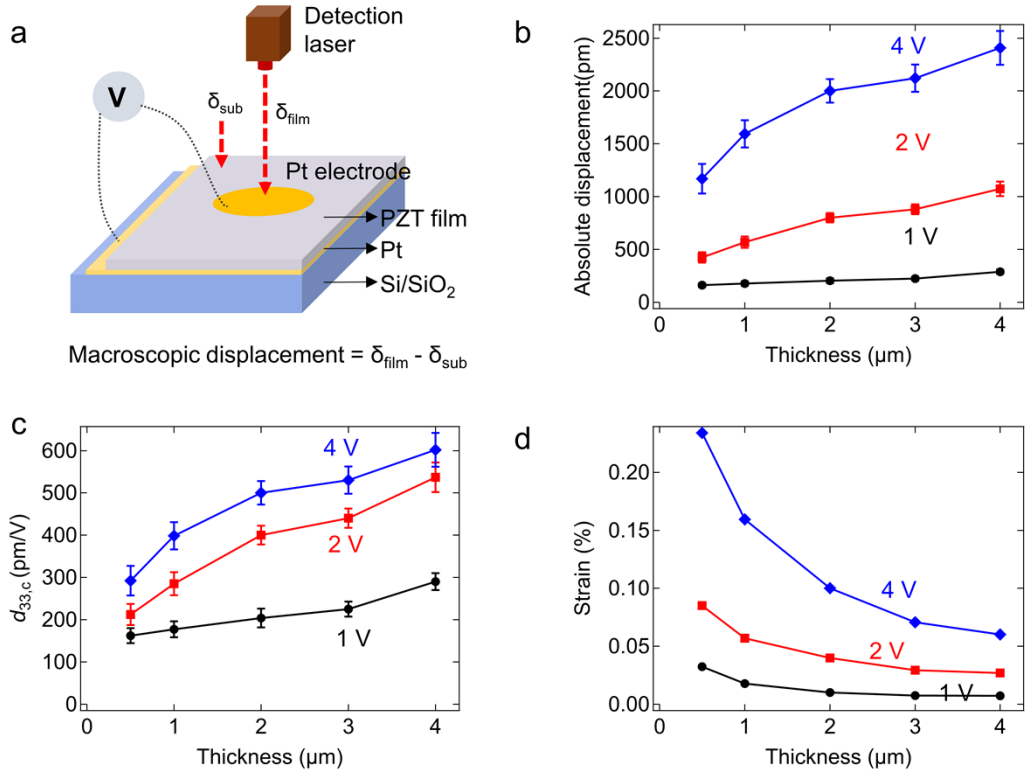

e

kV/cm	0.5	1	2	3	4
1 V	20	10	5	3	2.5
2 V	40	20	10	6	5
4 V	80	40	20	13	10
Ec	67	56	44	39	33

Supplementary Fig. 7. The converse piezoelectric coefficient $d_{33,c}$ of films with different thicknesses, as measured using a laser scanning vibrometer (LSV)[4,5]. a, Schematic of the measurement setup. The electrode used has a diameter of 2.5 mm, the same as that for direct piezoelectricity measurements. To rule out the bending effect in the measurements, the sample is adhered to the platform by silver paste, and both the displacement from the non-electroded area (i.e., the substrate displacement, δ_{sub}) and the electroded area (δ_{film}) are measured, with the effective displacement being obtained by subtracting the substrate value. **b and c,** The absolute displacement and calculated $d_{33,c}$ of the films as a function of thickness and applied AC bias. Note that normally DC bias above the coercive field is used to pole the film, while the superimposed AC bias is used to measure the displacement through LSV method. In the current work, to demonstrate its self-poling character, only AC bias constrained below 4 V with a frequency of 1 kHz is used. As anticipated, the self-poled film shows measurable

displacement even without any substantial external poling. However, the converse effect is significantly clamped by the substrate at a measuring bias of 1V. The clamping effect will be weakened with increasing bias voltage. Therefore, with slightly increasing bias to 4V, $d_{33,c}$ is greatly enhanced, reaching 293-602 pm/V for films with thicknesses ranging from 0.5 μm to 4 μm in thickness, being comparable to $d_{33,d}$. **d,** The calculated strain of the films at the bias of 4V. Notably, applying the same bias of 4V to films with increasing thickness will lead to reduced electric field and strain in the films. However, these strain values are reasonable for PZT films, considering that the applied fields are near or below their coercive fields as compared in panel **e.** This demonstrate the validity of these measurements.

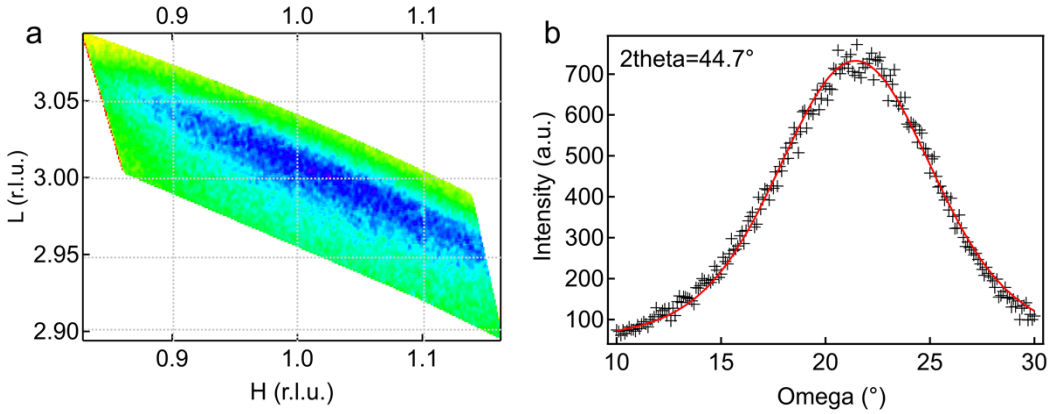

Supplementary Fig. 8. a, RSM mapping of (113) reflection. **b**, Rocking curve of (002) peak of 2 μm-thick textured PZT film. The black markers are experimental data and the red curve is a Gauss fitting of the experimental data. The RSM mapping of (113) shows an elongated pattern, while the rocking curve of (002) peak shows a rather broad character spanning from 10° to 30° Omega angle. These indicate the relative random in-plane orientation of the grains within the studied textured PZT films.

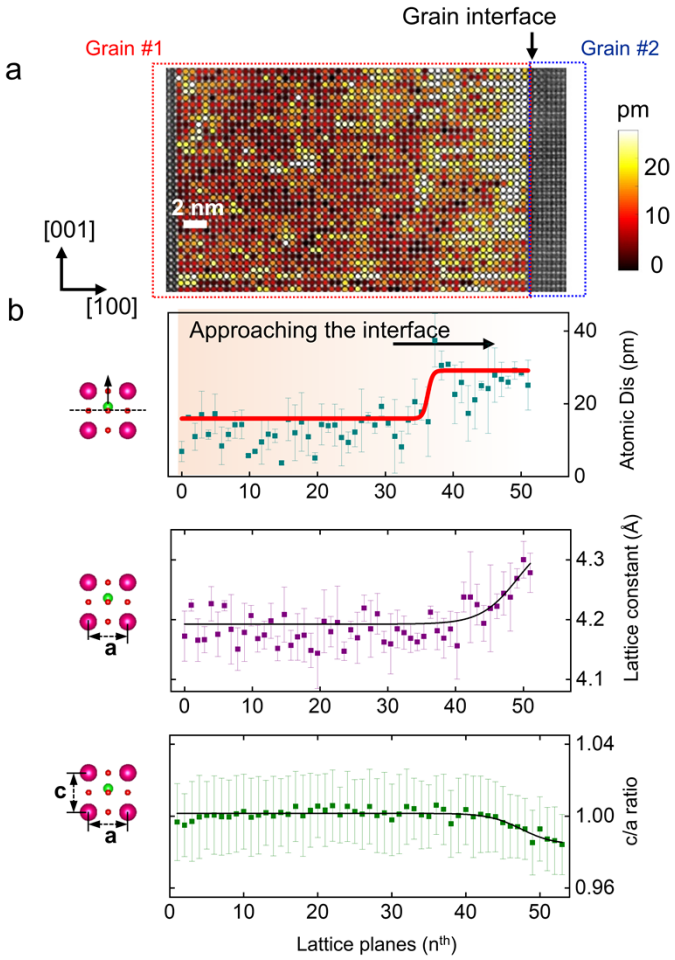

Supplementary Fig. 9. a, STEM-HAADF image of two adjacent grains with significant in-plane twist, showing the interfacial structure with the imposed atomic-scale displacement mapping for grain #1**. b**, Line profile of the atomic displacement, lattice parameter *a*, and *c*/*a* ratio are plotted as the function of the lattice planes approaching the interface of two twisted grains. The line profile is integrated from all data shown in panel a. The interface of grains and the enhancement point of the displacement are indicated by black arrows.

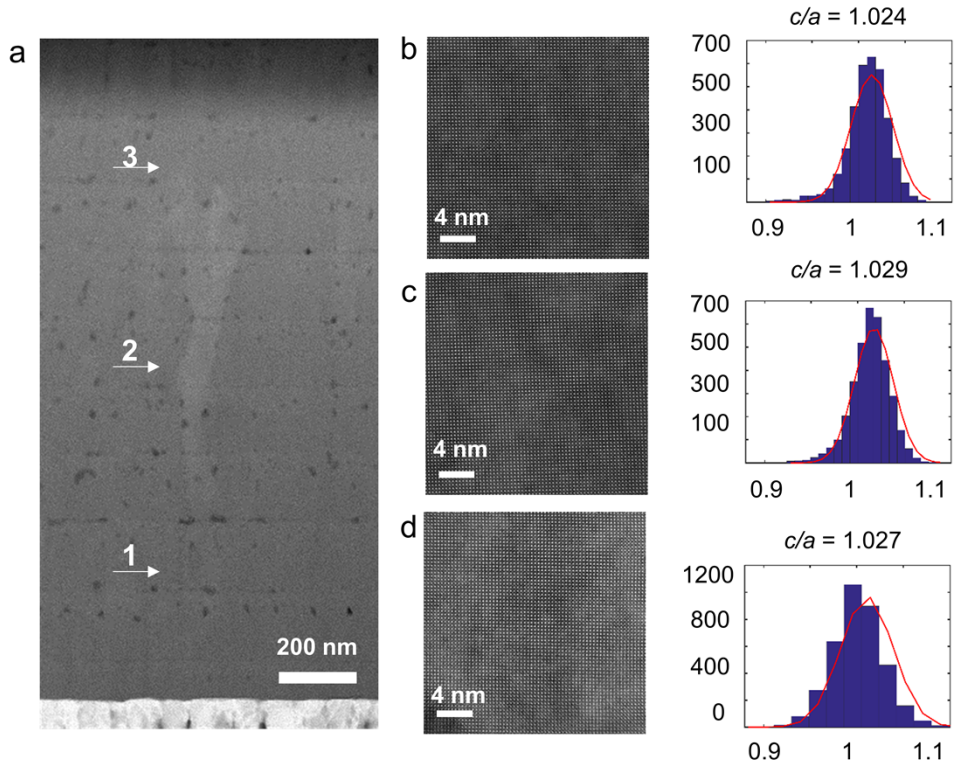

Supplementary Fig. 10. a, Low-magnification TEM image. **b-d**, HAADF-STEM images and quantified lattice parameters (*c/a* ratio) along the film thickness direction at regions near the bottom, in the middle, and at the surface areas of a textured PZT film, respectively. Panels b-d correspond to positions #1-3 as marked in panel a. The lattice parameters show negligible change at identical positions of each layer.

Supplementary Table 1 The lattice parameter of bulk PZT ceramics and PZT films with different Zr/Ti ratio on different substrates. Notably, the MPB and Ti-rich compositions of films on the silicon substrates are previously reported with rhombohedral and tetragonal coexistence[6].

	Lattice	30:70	40:60	52:48	70:30	Ref
Bulk	*c* (Å)	4.15	4.14	4.12	4.10	[7]
	a (Å)	3.99	4.02	4.08	4.10	
Film on Si (tensile stress on *a*)	*c* (Å)	4.12(T)	4.14(T)	4.14(T)	4.11	[6,8]
	a (Å)	4.00(T) 4.07(R)	4.02(T) 4.08(R)	4.07(T) 4.07(R)	4.11	
	c/a	~1.027	~1.022	~1.017	~1	
Film on STO (compressive stress on *a*)	*c* (Å)	-	4.18	4.15	4.15	[9]
	a (Å)	-	4.03	4.07	4.09	

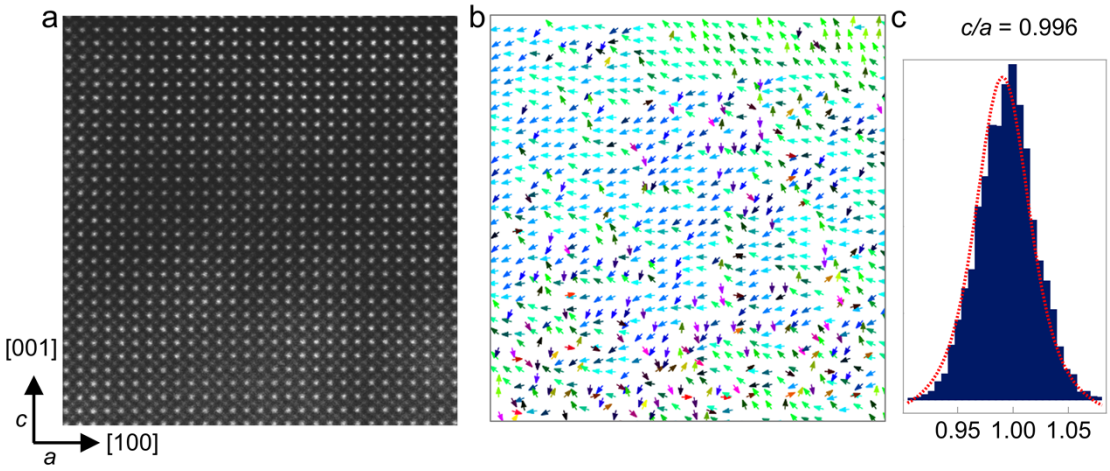

Supplementary Fig. 11. Ti-rich regions with less out-of-plane polarization alignments compared to that shown in the main text. a, STEM-HAADF images at selected Ti-rich regions. **b**, The maps of atomic-scale polarization as calculated from the *A*- and *B*-site atomic positions in corresponding STEM-HAADF images. **c,** Histogram of the *c*/*a* ratio.

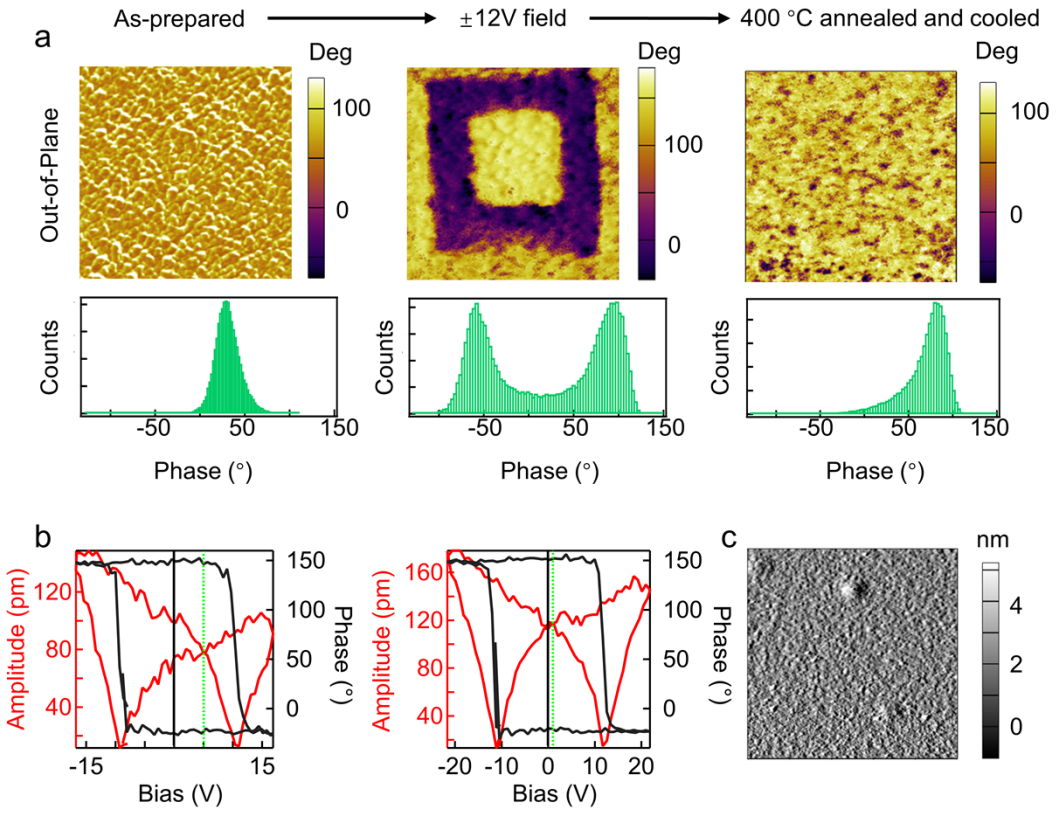

Supplementary Fig. 12. a, Out-of-Plane (OP) phase images as characterized by piezoresponse force microscopy (PFM) of the as-prepared PZT film, the film after poling using a field of ± 12 V through the PFM tip, and that after heating up to 400 °C followed by cooling down. Below each image is the histogram of the phase distribution. Notably, the polarizations are aligned in the as-prepared state with a single peak in the histogram (bottom of panel a). However, switching these polarizations using PFM tips with a voltage (e.g., ±12 V) is feasible, allowing for the creation of desirable written patterns. The written pattern can be erased by repeating the fabrication process, i.e., annealing the same sample under the fabrication temperature. This results in a recovery to an identical self-poling state as when it was initially prepared, with aligned polarizations observed again. This inherent self-poling nature not only eliminates the need for a pre-poling process but also allows the ferroelectric films to effectively retain its initial poled state even after exposure to high temperature. **b**, Local switching curve and phase at different fields. Note that at a smaller field, the switching curve shows an asymmetric characteristic, which gradually disappears as the applied field intensifies, ultimately leading to very small internal bias of only 1V in the films. It demonstrates the relative ease of polarization switching, consistent with the PFM scanning. **c**, Topographic images of the as-prepared PZT films as characterized by atomic force

microscopy (AFM) at the same area. The observed PFM responses are not impacted by artificial topographic effects, considering the corresponding smooth and well-defined topography in the AFM image. The area for the measurement is 4×4 μm. This is carried out on a 2 μm-thick PZT film for demonstration purposes.

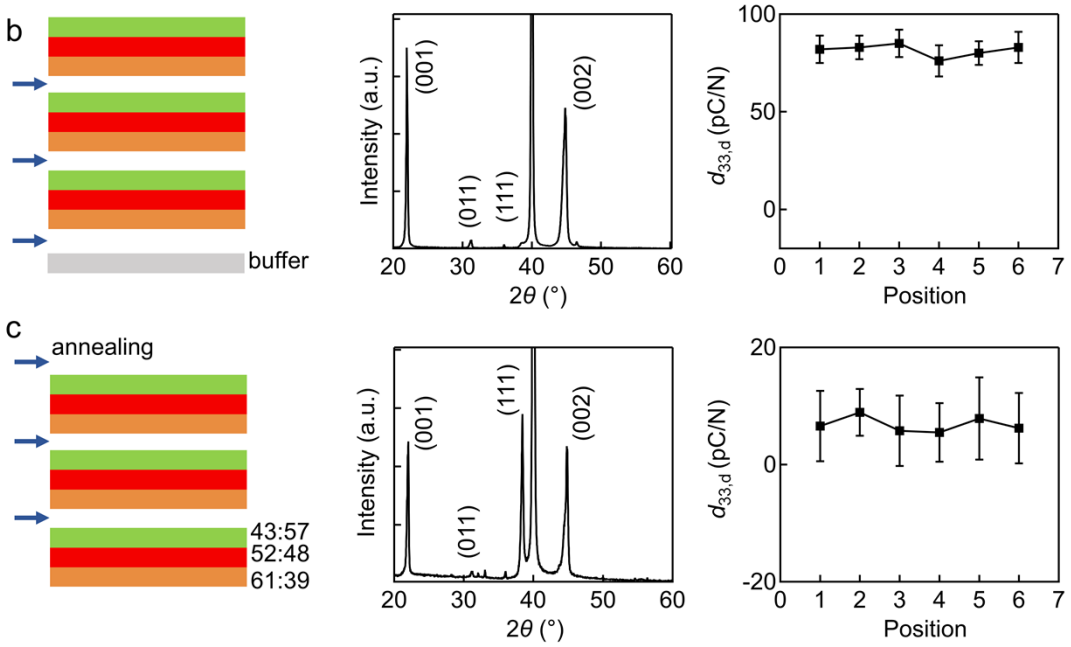

Supplementary Fig. 13. Comparative experiments of textured and non-textured PZT films with suppressed Zr/Ti segregation. a, The schematic of depositing [001]-textured PZT films with suppressed Zr/Ti segregation, with XRD pattern and the macroscopic piezoelectricity. The blue arrows in the schematic denote for the annealing process. The buffer layer is PbO-TiO_2 with a ratio of 83:17 for achieving [001] texture. Considering different growth rates of Zr-rich and Ti-rich compositions, a periodic Zr/Ti from 61:39, to 52:48, to 43:57, is annealed together, suppressing Zr/Ti segregation during the crystallization (see Methods). However, the Zr/Ti segregation is possibly not completely eliminated using this method, thus, the macroscopic piezoelectricity is greatly reduced, but is still 80 pC/N. **b**, The schematic of depositing non-textured PZT films with suppressed Zr/Ti segregation using a same compensating annealing method, with XRD patterns and the macroscopic piezoelectricity. The $d_{33,d}$ values of for these films are < 10 pC/N. This comes from the following possible reasons: (i) The X-ray diffraction (XRD) pattern of non-buffered PZT films exhibited comparable peak intensities of (001), (111), and (002) reflections, showing a weak [001] texture with a Lotgering factor of ~50%; and (ii) Zr/Ti segregation is not completely eliminated as described above.

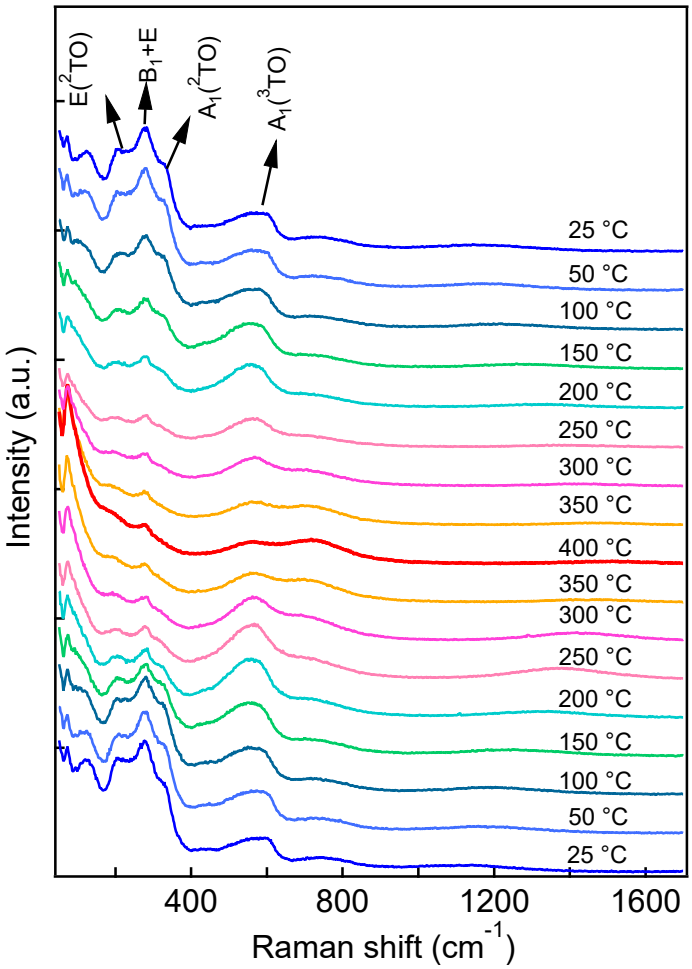

Supplementary Fig. 14. Temperature-dependent Raman spectra of 2 μm-thick PZT film. At room temperature, E(^{2}TO), B_1 + E, and A_1(^{2}TO) phonon modes at 200, 275, and 325 cm^{-1}, and A_1(^{3}TO) mode at 560 cm^{-1} demonstrate ferroelectric character and tetragonal-like structure of the studied PZT[10]. These modes weaken or disappear on heating, indicating the phase transition of polar to nonpolar phases. The Raman spectra also demonstrate well-recovered vibration modes after cooling back to room temperature.

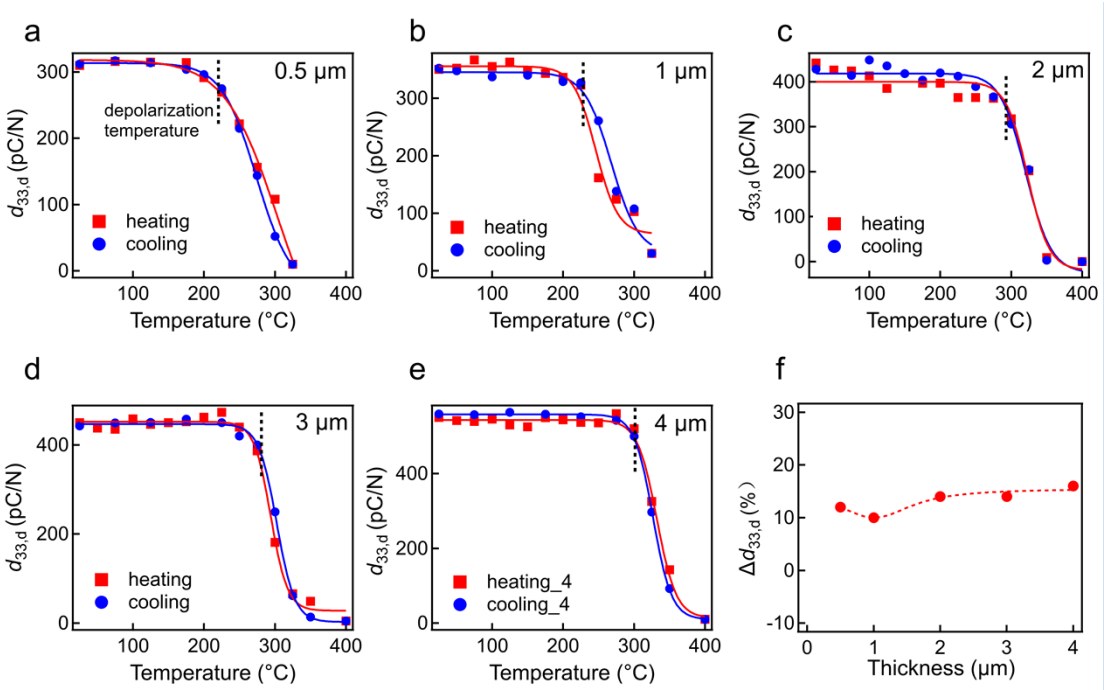

Supplementary Fig. 15. a-e, Thermal stability of PZT films with thicknesses of 0.5, 1, 2, 3, and 4 μm. The depolarization temperature for each film is indicated by black vertical dashed lines. **f,** Extracted piezoelectric property variation up to their depolarization temperatures as a function of film thickness. The different PZT films sets exhibit variations in piezoelectric properties ($\Delta d_{33,d}/d_{33,d}$) ranging from 10% to 16%, with negligible thermal hysteresis during both upward and downward temperature sweeps. The depolarization temperature increases from 220 °C (for 0.5 - 1 μm film) to approximately 300 °C (for 2-4 μm films). This variation is likely due to the more significant thermal stress or stress gradient in thinner films, which could impact its built-in fields and damage $d_{33,\,d}$ at elevated temperatures.

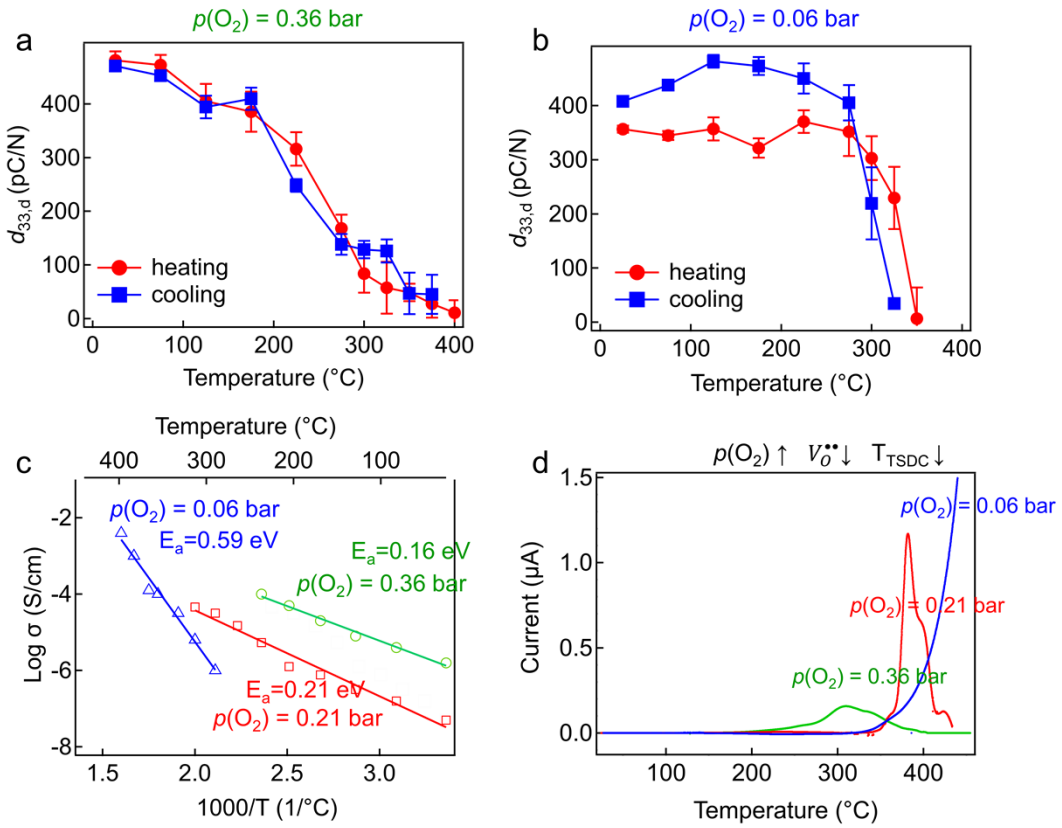

Supplementary Fig. 16. a and **b**, Self-poled Piezoelectricity of PZT films annealed under different oxygen pressure. **c**, DC electric conductivity versus inverse of temperature (Arrhenius plot) of PZT film annealed under different oxygen partial pressures, where E_a represents the activation energy. **d**, Thermally stimulated depolarization currents as observed for films post-treated under different oxygen partial pressures. The stability deteriorates in samples annealed under higher oxygen partial pressure, $p(O_2)$ from 0.21 bar to 0.36 bar, but remains robust for those subjected to decreased $p(O_2)$ to 0.06 bar. The primary impact is the oxygen vacancy levels. It can be concluded that these vacancies and the electrons ($V_O^{\bullet\bullet} + 2e' \rightarrow O_O^X$) occurs under oxygen-rich conditions, leading to an increase in the number of free holes in the studied film. Consequently its transport behavior at elevated temperatures can be determined by oxygen vacancies, which had been confirmed by the Arrhenius plot. The plot shows that the studied PZT is a *p*-type semiconductor with an activation energy (E_a) of 0.16 or 0.21 eV when annealed under 0.36 bar or 0.21 bar $p(O_2)$, respectively. In contrast, it exhibits ionic conductor characteristics with $E_a \sim 0.59$ eV when annealing under 0.06 bar $p(O_2)$. The thermally stimulated depolarization current (TSDC) also serves as a valuable method to study the polarized status of ferroelectrics, which is associated with the migration of oxygen vacancies. TSDC relaxation peaks appear at respective

temperatures of ~308, 381, and above 400 °C, for the samples subjected to different oxygen partial pressures. As $p(O_2)$ increases and oxygen vacancy concentration decreases in the film, the depolarization relaxation peak shifts to lower temperatures, compromising its thermal stability. It is expected that the transformation to a *p*-type semiconductor with free holes will alter the polarization configuration at elevated temperatures, thereby deteriorating the thermal stability of the self-poled piezoelectricity, while a specific amount of oxygen vacancies in films treated under oxygen-deficient conditions is beneficial to the thermal stability.

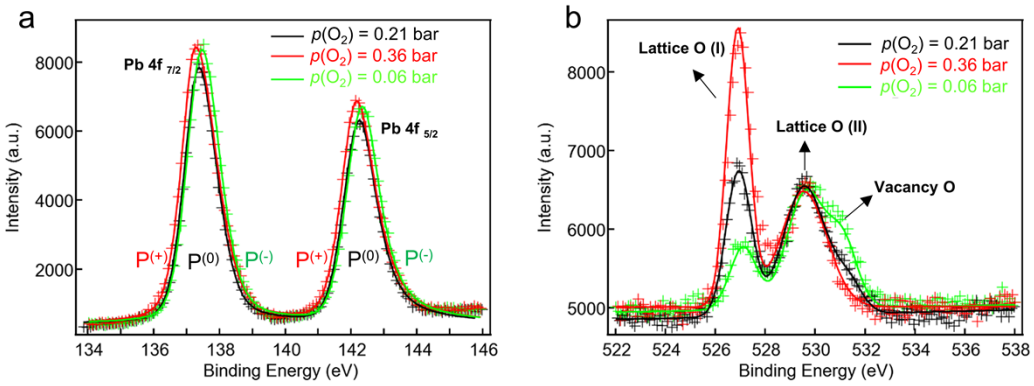

c

	Peak Position		Peak Intensity	
	Pb 4f $_{7/2}$	Pb 4f $_{5/2}$	Lattice O (II)	Vacancy O
$p(O_2)$ = 0.21 bar	137.37	142.25	3512.8	501.5
$p(O_2)$ = 0.36 bar	137.27	142.17	3411.5	112.5
$p(O_2)$ = 0.06 bar	137.46	142.34	2858.6	1149.2

Supplementary Fig. 17. a and **b**, X-ray photoelectron spectra (XPS)**. c**, Peak position and intensity of Pb and O peak for PZT films annealed under different oxygen pressure. During the annealing treatment in different atmospheres, Pb and O elements might suffer the most profound effect due to Pb volatilization and O injection. The O vacancy shoulder peak greatly reduces in intensity after annealing in an oxygen-rich atmosphere [11] and greatly increases for that annealed in oxygen-poor atmosphere as expected. The main component of Pb belongs to areas with no surface band bending and is denoted as P(0), the charge carrier dynamics near the surface (especially the holes induced by the photoemission process) may alter the relative weight of P(+) and P(-) areas [11]. The shift of the Pb position towards a higher binding energies for that annealed in N_2 (green curve) means a reinforced P(+) state at the surface. This is consistent with the self-poling direction of the investigated film. For $p(O_2)$ = 0.36 bar annealing, it is more complex, the peaks expanded to both the higher binding energy side and the lower binding energy side (red curve). Which at the same time show a reinforcing of the P+, the depolarizing field, and the generation of possible P- (implies an unstable depolarizing field). Thus the thermal stability becomes worse. However, the further Pb volatilization maybe reinforced in the PZT film, resulting in internal field related to defects and thus explaining the enhanced d_{33}.

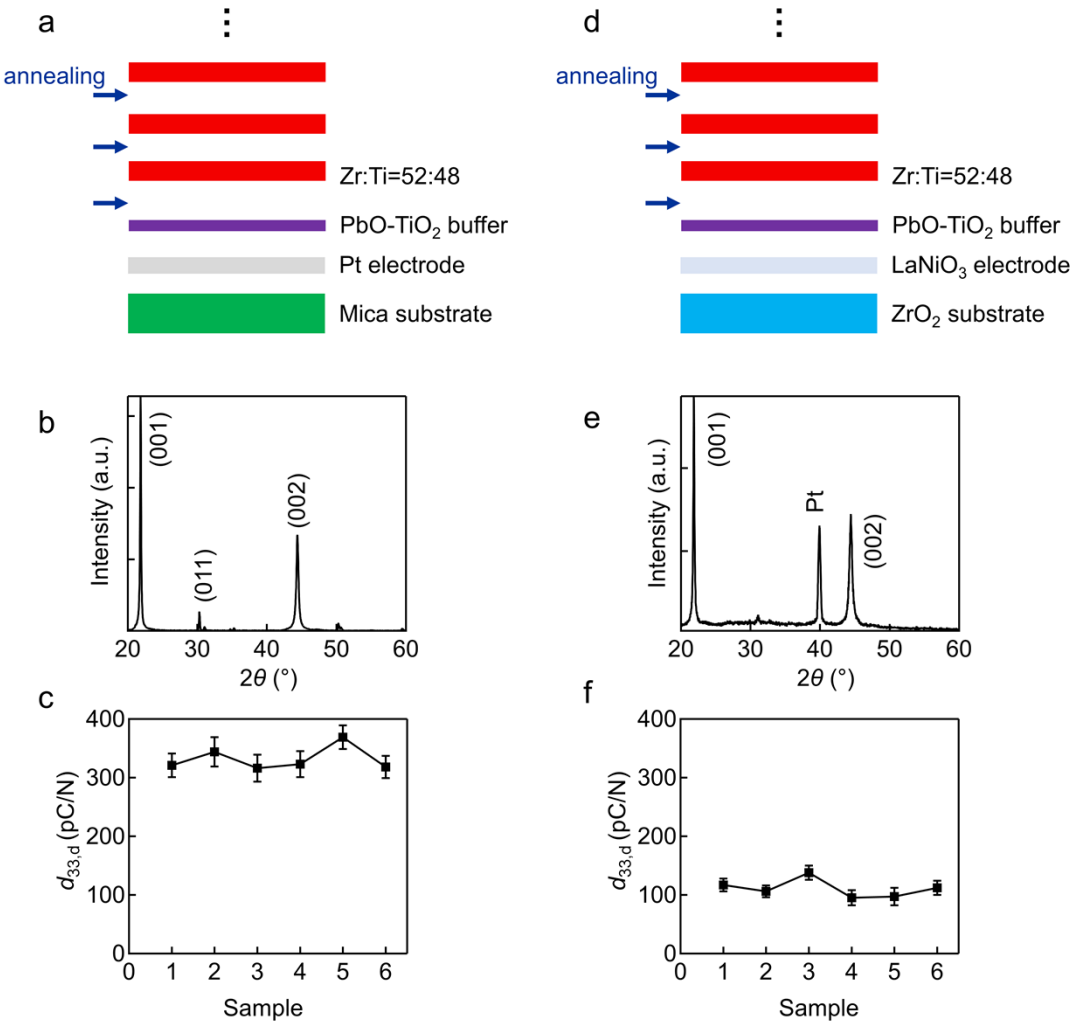

Supplementary Fig. 18. Validation of the proposed two-step approach for achieving macroscopic $d_{33,d}$ on Mica and ZrO_2 substrates. a, Schematic illustrating the deposition of [001]-textured PZT films with controlled Zr/Ti segregation using a PbO-TiO_2 buffer layer as shown in the main text on a Mica substrate. A 100 nm Pt electrode was deposited by *rf* magnetron sputtering. **b,** XRD pattern of PZT/Pt/Mica, confirming the [001] texture of the film. **c,** $d_{33,d}$ values measured across six samples deposited on Mica substrates. **d,** Schematic of the deposition of [001]-textured PZT films with controlled Zr/Ti segregation using a PbO-TiO_2 buffer layer as shown in the main text on ZrO_2. A 100 nm $LaNiO_3$ (LNO) was deposited via sol-gel method as the bottom electrode (Note that the Pt electrode tends to peel off easily on ZrO_2). **e,** XRD pattern of PZT/LNO/ZrO_2, confirming the [001] texture of the film. **f,** $d_{33,d}$ values measured across six samples deposited on ZrO_2 substrate. The measurable macroscopic properties validate the effectiveness of the proposed two-step approach for achieving self-poling.

References

1 Pan, Z. *et al.* Achieving high discharge energy density and efficiency with NBT-based ceramics for application in capacitors. *J. Mater. Chem. C* **7**, 4072 (2019).

2 Zhou, Z. *et al.* Textured $Bi_{1/2}Na_{1/2}TiO_3$-$BaTiO_3$ lead-free films with enhanced piezoelectric property and depolarization temperature. *Adv. Electron. Mater.* **4**, 1800351 (2018).

3 Huang, Y. *et al.* Simultaneously achieved high- energy storage density and efficiency in (K,Na)NbO_3- based lead- free ferroelectric films. *J. Am. Ceram. Soc.* **104**, 4119–4130 (2021).

4 Yao, K. & Tay, F. E. H. Measurement of Longitudinal Piezoelectric Coefficient of Thin Films by a Laser-Scanning Vibrometer. *IEEE Trans. Ultrason. Ferroelectr. Freq. Control* **50**, 113-116 (2003).

5 Herdier, R., Dogheche, D. J. E., Rèmiens, D. & Sulc, M. Laser Doppler vibrometry for evaluating the piezoelectric coefficient on thin film. *Rev. Sci. Instrum.* **77**, 093905 (2006).

6 Cheng, C., Peters, T. & Trolier-McKinstry, S. Cracking behavior in lead zirconate titanate films with different Zr/Ti ratios. *Appl. Phys. Lett.* **121**, 162907 (2022).

7 Chung, C.-C. Microstructural Evolution in Lead Zirconate Titanate (PZT) Piezoelectric Ceramics. *Doctoral Dissertations* (2014).

8 Khaenamkaew, P., Muensit, S., Bdikin, I. K. & Kholkin, A. L. Effect of Zr/Ti ratio on the microstructure and ferroelectric properties of lead zirconate titanate thin films. *Materials Chemistry and Physics* **102** 159–164 (2007).

9 Kanno, I. *et al.* Crystallographic characterization of epitaxial films with different Pb (Zr , Ti)O3 *J. Appl. Phys. 93, (2003)* **93**, 4091–4096 (2003).

10 Pontes, D. S. L. *et al.* Synthesis, optical and ferroelectric properties of PZT thin films: experimental and theoretical investigation. *J. Mater. Chem.* **22**, 6587-6596 (2012).

11 Pintilie, L. *et al.* Polarization induced self-doping in epitaxial $Pb(Zr_{0.20}Ti_{0.80})O_3$ thin films. *Scientific Reports* **5**, 14974 (2015).